



ELSEVIER

Contents lists available at ScienceDirect

## Earth and Planetary Science Letters

journal homepage: [www.elsevier.com/locate/epsl](http://www.elsevier.com/locate/epsl)

## Frictional power dissipation in a seismic ancient fault

Francesco Lazari<sup>a,1</sup>, Angela Castagna<sup>b</sup>, Stefan Nielsen<sup>c</sup>, Ashley Griffith<sup>d</sup>,  
Giorgio Pennacchioni<sup>a</sup>, Rodrigo Gomila<sup>a</sup>, Phil Resor<sup>e</sup>, Chiara Cornelio<sup>f</sup>, Giulio Di Toro<sup>a,f,\*</sup>

<sup>a</sup> Dipartimento di Geoscienze, Università degli Studi di Padova, Padua, Italy<sup>b</sup> School of Geography, Geology and the Environment, Leicester University, United Kingdom<sup>c</sup> Department of Earth Sciences, Durham University, Durham, United Kingdom<sup>d</sup> School of Earth Sciences, The Ohio State University, Columbus, OH, USA<sup>e</sup> Department of Earth and Environmental Sciences, Wesleyan University, Middletown, CT, USA<sup>f</sup> Sezione Roma 1, Istituto Nazionale di Geofisica e Vulcanologia, Rome, Italy

## ARTICLE INFO

## Article history:

Received 15 October 2022

Received in revised form 6 February 2023

Accepted 13 February 2023

Available online 27 February 2023

Editor: R. Bendick

Dataset link: [https://](https://researchdata.cab.unipd.it/id/eprint/725)[researchdata.cab.unipd.it/id/eprint/725](https://researchdata.cab.unipd.it/id/eprint/725)

## Keywords:

earthquake

faults

frictional power

pseudotachylyte

rock friction experiments

## ABSTRACT

The frictional power per unit area  $\dot{Q}$  (product of frictional traction  $\tau$  and slip rate  $\dot{u}$  in  $\text{MW m}^{-2}$ ) dissipated during earthquakes triggers fault dynamic weakening mechanisms that control rupture nucleation, propagation and arrest. Although of great relevance in earthquake mechanics,  $\dot{Q}$  cannot, with rare exceptions, be determined by geophysical methods. Here we exploit theoretical, experimental and geological constraints to estimate  $\dot{Q}$  dissipated on a fault patch exhumed from 7–9 km depth. According to theoretical models, in polymineralic, silicate rocks the amplitude ( $< 1$  mm) of the grain-scale roughness of the boundary between frictional melt (pseudotachylyte) and host rock decreases with increasing  $\dot{Q}$ . The dependence of grain-scale roughness with  $\dot{Q}$  is due to differential melt front migration in the host rock minerals. This dependence is confirmed by friction experiments reproducing seismic slip where pseudotachylytes were produced by shearing tonalite at  $\dot{Q}$  ranging from 5 to 25  $\text{MW m}^{-2}$ . In natural pseudotachylytes across tonalites, the grain-scale roughness broadly decreases from extensional to compressional fault domains where lower and higher  $\dot{Q}$  are expected, respectively. Analysis of the natural dataset calibrated by experiments yields  $\dot{Q}$  values in the range of 4–60  $\text{MW m}^{-2}$  (16  $\text{MW m}^{-2}$  average value). These values, estimated in small fault patches, are at the lower end of broad estimates of  $\dot{Q}$  (3–300  $\text{MW m}^{-2}$ ) obtained from frictional tractions (30–300 MPa) and fault slip rates (0.1–1 m/s) assumed as typical of upper crustal earthquakes.

© 2023 Elsevier B.V. All rights reserved.

## 1. Introduction

Frictional power dissipation per unit area ( $\dot{Q}(t) = \tau(t) \dot{u}(t)$  in  $\text{W m}^{-2}$ , or  $\text{Nm s}^{-1} \text{m}^{-2}$  in units commonly used in geodesy and seismology, with:  $\tau$  frictional traction or shear stress;  $\dot{u}$  on-fault slip rate) is a relevant earthquake source parameter (Sibson, 1980). In fact,  $\dot{Q}(t)$  results in temperature increase and grain comminution in  $\mu\text{m}$ - to  $\text{cm}$ -thick slipping zones (Sibson, 2003), that activate dynamic weakening mechanisms promoting propagation of seismic ruptures (Rice, 2006; Di Toro et al., 2011; Tullis, 2015; Pozzi et al., 2021). However,  $\tau(t)$ , or the absolute value of frictional traction during seismic slip is transparent, with notable exceptions, to measurements from the Earth's surface (Gatterti and Spudich, 1998;

Udias et al., 2014). In fact, only the stress drop, not  $\tau(t)$ , has direct impact on  $\dot{u}(t)$  and therefore influences the seismological signature in the radiated waves (Udias et al., 2014). Instead, the absolute stress levels, and hence  $\tau(t) \dot{u}(t)$ , could be estimated by inversion analysis (1) from seismic waves if there is a visible rake rotation during seismic slip (Spudich, 1992) and, (2) as recently proposed, with geodetic techniques, from coseismic slip vectors measured along earthquake surface ruptures (Milliner et al., 2022). However, the two above remain exceptional cases. As a consequence, values of  $\dot{Q}(t)$  ranging from 3 to 300  $\text{MW m}^{-2}$  have been proposed assuming  $\tau$  and  $\dot{u}$  for ideal earthquakes in the continental crust and ranging from 30 to 300 MPa and 0.1 to 1  $\text{m s}^{-1}$ , respectively (Fig. 2 in Sibson, 1980). In this study we aim to obtain more rigorous estimates of  $\dot{Q}(t)$ , which controls the fault strength evolution during the earthquake in the presence of thermal weakening processes, from microstructural analysis of tectonic pseudotachylytes.

Tectonic pseudotachylytes are solidified friction melts produced during seismic faulting (Sibson, 1975). Pseudotachylytes have been

\* Corresponding author at: Dipartimento di Geoscienze, Università degli Studi di Padova, Padua, Italy.

E-mail address: [giulio.ditoro@unipd.it](mailto:giulio.ditoro@unipd.it) (G. Di Toro).

<sup>1</sup> Now at EPFL, Lausanne, Switzerland.

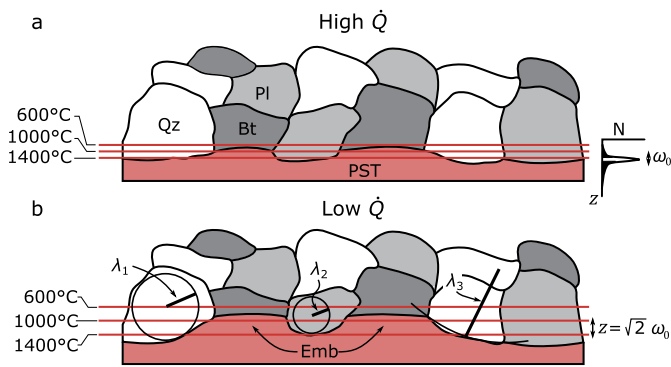


**Fig. 1.** Conceptual model of the relation between frictional power dissipation ( $\dot{Q}$ ) and grain-scale roughness of the boundary between melt (PST, pseudotachylyte once solidified) and host rock (HR) during seismic slip in a granitoid (Qz = quartz;  $T_m \sim 1730^\circ\text{C}$ ; Bt = biotite;  $T_m \sim 650^\circ\text{C}$ ; Pl = plagioclase An<sub>45</sub>;  $T_m \sim 1250^\circ\text{C}$ ; Navrotsky, 1995; Spray, 2010; Deer et al., 1992). Red lines represent isotherms with decreasing spacing with increasing  $\dot{Q}$ . **(a)** High  $\dot{Q}$ : the thermal gradient is high; the host rock minerals melt almost at the same rate resulting in a relatively smooth PST-HR boundary. **(b)** Low  $\dot{Q}$ : the thermal gradient is low and biotite is more affected by melting than the other minerals; as result deep embayments (Emb) and a rugged PST-HR boundary develop. The grain-scale roughness of the PST-HR boundary is described by  $\omega_0$  (characteristic asperity height, Eq. (1)) and  $\lambda_{ave}$  (average radius of the asperities, Eq. (2)). The distance  $z = \sqrt{2} \omega_0$  corresponds to the depth of the embayments (see also methods section). In this conceptual model, the thermal diffusivity of melt and wall rocks is the same and latent heat of fusion is not considered; the isotherms are approximated as planes for simplicity. In reality, different thermal diffusivities and the latent heat of fusion exchanged during mineral melting may perturb the parallelism of the isotherms. Modified from Nielsen et al. (2010).

used to estimate several earthquake source parameters, including the magnitude of frictional traction, rupture directivity, slip weakening distance, energy budgets, focal mechanisms, stress drops, apparent stress, fracture energy, measures of efficiency and hypocentral depths (Sibson, 1975; Maddock et al., 1987; Di Toro et al., 2005, 2006; Hirose and Shimamoto, 2005; Andersen et al., 2008; Pittarello et al., 2008; Beeler et al., 2016; Petley-Ragan et al., 2019; Ferrand et al., 2021; Johnson et al., 2021; Hosseinzadehsabeti et al., 2021). During earthquakes, seismic rupture propagation (at a few km/s) induces intense and abrupt near-tip stress perturbations that result in host rock fracturing, grain comminution and flash heating (Reches and Dewers, 2005; Rice, 2006). In silicate rocks, fault slip may result in temperature increase and frictional melting of the comminuted materials and their host rocks close to the fault surface (Swanson, 1992; Spray, 1995). At this stage and in the few seconds following seismic slip, the melt-rock boundary migrates into the host rocks (Fialko and Khazan, 2005; Nielsen et al., 2008). The melt intrudes fractures in the host rocks (injection veins) or flows along the fault towards dilatational jogs and reservoirs (fault veins) (Sibson, 1975). In the case of granitoid rocks, made of feldspars, quartz and biotite, this ultra-fast melting occurs under non-equilibrium conditions (Shand, 1916). Along the migrating melt-rock boundary, minerals with low melting temperature  $T_m$  (biotite,  $T_m \sim 650^\circ\text{C}$ , Navrotsky, 1995) melt faster than high  $T_m$  minerals (for andesine feldspar, An<sub>45</sub>, and quartz,  $T_m \sim 1250^\circ\text{C}$  and  $T_m \sim 1730^\circ\text{C}$ , respectively, Navrotsky, 1995; Spray, 2010). Differential mineral melting results in a grain-scale roughness of the melt-rock boundary (or pseudotachylyte-host rock boundary, from now on PST-HR, once the melt solidifies): embayments and protrusions form in spatial relation with HR biotite and quartz/feldspar grains, respectively (Magloughlin and Spray, 1992, and references therein) (Fig. 1). The grain-scale roughness is related to (i) mineral physical properties ( $T_m$  and thermal shock properties: Papa et al., 2018) and grain size; (ii) melt temperature; and (iii) rate of the temperature increase in the slipping zone, proportional to  $\dot{Q}$ . Theoretical analysis, tested by experiments on gabbro, indicates

that the higher the  $\dot{Q}$ , the smoother the PST-HR boundary (Nielsen et al., 2010) (Fig. 1). Here we measure the grain-scale roughness of the PST-HR boundary of natural pseudotachylytes within the Adamello granitoids (tonalite) along the Gole Larghe Fault Zone (Italian Southern Alps; Di Toro and Pennacchioni, 2005). After calibration with dedicated experiments, we estimate  $\dot{Q}$ .

## 2. Methods

**Experimental pseudotachylytes** were produced by shearing hollow cylinders (50/30 mm external/internal diameter) of non-altered Adamello tonalite with the rotary machine SHIVA installed at the Istituto Nazionale di Geofisica e Vulcanologia in Rome (Di Toro et al., 2010; for sample preparation see Nielsen et al., 2012). Three experiments (S422, S423 and S475) were conducted at room humidity conditions, target equivalent slip rates  $V_{eq}$  of  $6.5 \text{ m s}^{-1}$  and normal stresses of 40, 20, 30 MPa, respectively (Fig. 2, Table 1). During the experiments, normal stress, torque (converted into  $\tau$ ), angular rotations and speeds (converted into equivalent slip distances and slip rates, respectively), and sample shortening were measured at acquisition rates of 2.5 kHz (see Niemeijer et al., 2011 for details about the calibration and data acquisition). We also examined a fourth pseudotachylyte produced in previously published experiments performed on the same Adamello tonalite. This pseudotachylyte was obtained by shearing full cylinders, 25 mm in diameter, at equivalent slip rate of  $1.3 \text{ m s}^{-1}$  and 20 MPa normal stress using a rotary apparatus at Kyoto University (HVR377 in Di Toro et al., 2006). The temperature evolution with slip displacement in the slipping zone was estimated with 2-dimensional numerical modeling (Supplementary Materials SM1, Cornelio et al., 2019).

**Natural pseudotachylytes.** 22 samples were collected from eight pseudotachylyte-bearing wavy faults from the dextral strike-slip Gole Larghe Fault Zone (Di Toro and Pennacchioni, 2005) within the Adamello batholith (Callegari and Brack, 2002). The granitoid rock (tonalite) consists of plagioclase (i.e., andesine, An<sub>45</sub>, 48% modal composition), quartz (29%), biotite (17%) and K-feldspar (6%) with an average grain size of 2 mm (Di Toro and Pennacchioni, 2004; 2005). The fault zone was exhumed from 7–9 km depth and is made of  $\sim 200$  main sub-parallel, exceptionally exposed faults (Di Toro and Pennacchioni, 2005; Mitterpergher et al., 2021; Smith et al., 2013). Pseudotachylytes were collected from extensional, neutral and compressional structural domains along wavy fault veins and from injection veins (opening mode cracks) (Fig. 3a). The injection veins are asymmetrically distributed and mostly intruded the south-facing wall rock (Di Toro et al., 2005).

**Thin sections.** 22 natural and three experimental pseudotachylytes were cut perpendicular to the slip zone and parallel to the slip direction (see Supplementary Materials SM2 for the digital scans of the thin sections). The derived  $\sim 30 \mu\text{m}$  thick thin sections were Syton<sup>®</sup>-polished for high resolution FESEM and EMPA analysis.

**Microstructural analysis** was performed with an optical petrographic microscope and with a high-resolution Tescan Solaris Field Emission Scanning Electron Microscope (FESEM) at the Dept. of Geosciences in University of Padova. Back Scatter Electrons (BSE) and Cathodoluminescence (CL) imaging were performed at the FESEM with operating conditions of: 14 mm working distance; 10 keV acceleration voltage; and 3 nA beam current.

**Elemental analysis** (composition of the pseudotachylyte matrix) was performed with electron wavelength-dispersive microprobe analysis (EMPA) on Syton<sup>®</sup>-polished thin sections at the Dept. of Geosciences in University of Padova. Data were collected using 15 kV as accelerating voltage and 15 nA as beam current. The analyzed volume of the thin section was 2–3  $\mu\text{m}$  in diameter. Sodium and

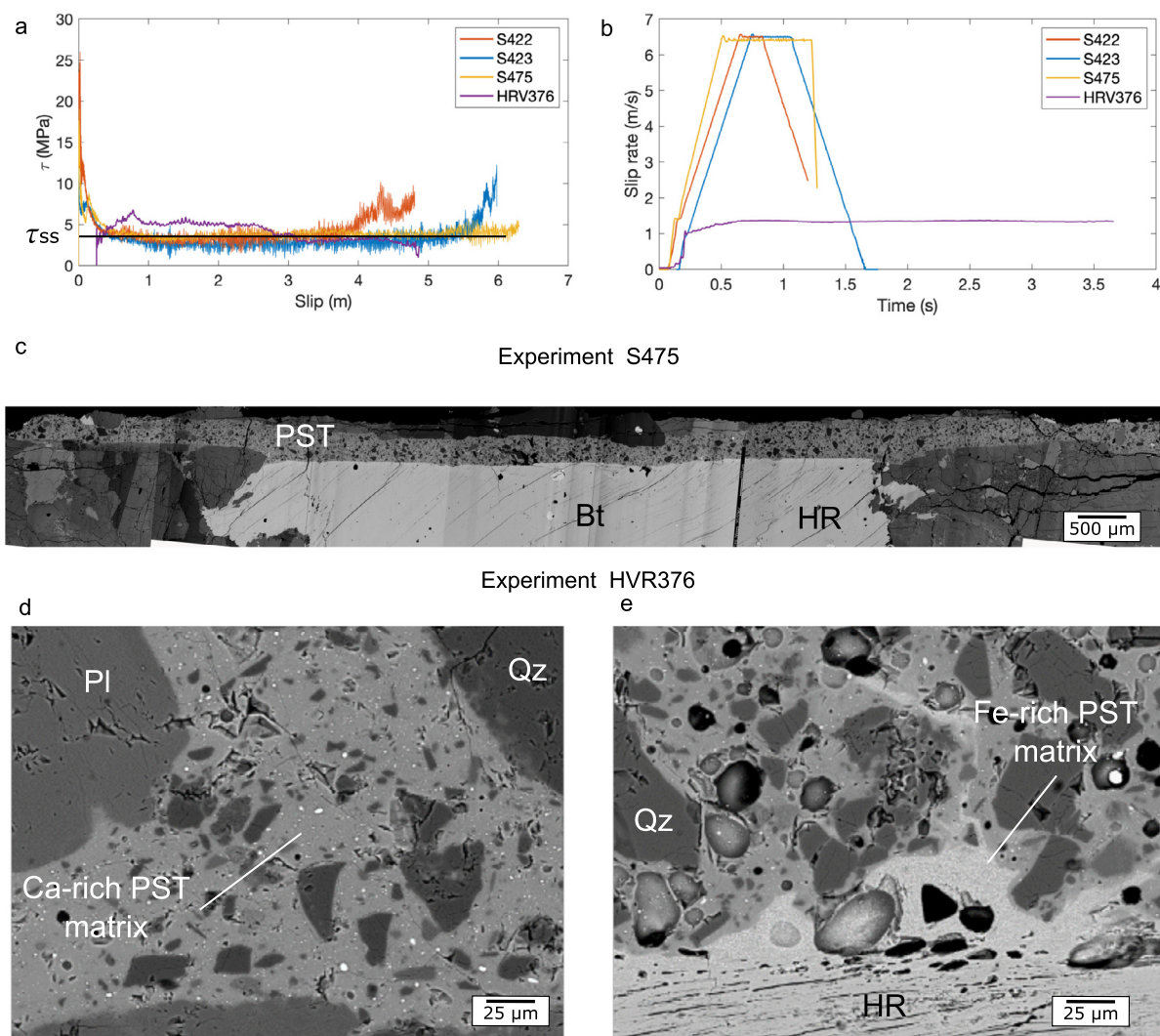


**Fig. 2.** Experimental pseudotachyrites and experimental data. **(a)** Evolution of frictional traction  $\tau$  vs. slip distance during experiments. The black in color segment defines  $\tau_{ss}$  for experiment S475. **(b)** Velocity function imposed to the samples in the four experiments. **(c)** Photomosaic of BSE-FESEM images of experiment S475 performed at 30 MPa normal stress. The  $\sim 3$  mm long embayment is in correspondence of the biotite grain. **(d)** Pseudotachylyte of experiment HVR376 with abundant angular clasts of quartz and few rounded clasts of plagioclase (andesine or  $\text{An}_{45}$  in composition) immersed in a Ca-rich glassy matrix. **(e)** Pseudotachylyte-host rock (PST-HR) boundary of experiment HVR376 with evidence of melting and dehydration (elongated vesicles) of biotite grains. A Fe-rich glassy matrix departs from the biotite (c to e, BSE-FESEM images. PST, pseudotachylyte; Bt, Biotite; HR, host rock; Pl, plagioclase; Qz, quartz).

**Table 1**

Experimental data: target velocity, imposed normal stress, measured peak and steady-state shear stress and calculated power dissipation per unit area. (\*) experiment published in Di Toro et al., 2006.

Experiment	Target velocity $V_{eq,ss}$ (m s <sup>-1</sup> )	Normal stress $\sigma_n$ (MPa)	Peak shear stress $\tau_p$ (MPa)	Steady-state shear stress $\tau_{ss}$ (MPa)	Power per unit area $\dot{Q}_{ss} = \tau_{ss} V_{eq,ss}$ (MW m <sup>-2</sup> )
HRV376*	1.3	20	6.784	3.86	5.02
S422	6.5	40	26.04	3.44	22.36
S423	6.5	20	12.29	2.70	17.55
S475	6.5	30	19.05	3.92	25.50

potassium were analyzed first to prevent alkali migration effects. The precision of the microprobe was measured through the analysis of well-characterized synthetic oxide and mineral secondary standards and was better than 5% for all cations.

**Grain-scale fault roughness analysis.** High resolution images (10  $\mu\text{m}$  pixel) of the entire thin section were obtained by optical (natural pseudotachylytes) and FESEM-BSE (experimental pseudotachylytes) imaging. The PST-HR boundaries of both natural and experimental pseudotachylytes were manually drawn with Inkscape® over a length ranging from 6.7 to 34.5 mm and with resolution of 10  $\mu\text{m}$

(see Supplementary Materials SM2). The resolution of the measurements (10  $\mu\text{m}$ , well below the average mineral grain size,  $\sim 2$  mm) and the length of the digitized PST-HR boundaries (greater than mineral grain size) allowed us to test whether the mineral grain size, together with  $\dot{Q}(t)$ , controls the grain-scale roughness of the PST-HR boundaries. The grain-scale roughness of the PST-HR boundaries was then analyzed with a MATLAB script to determine the Fast Fourier Transform (FFT) spectra,  $\omega_0$  (characteristic asperity height which corresponds to the root mean square, RMS, of

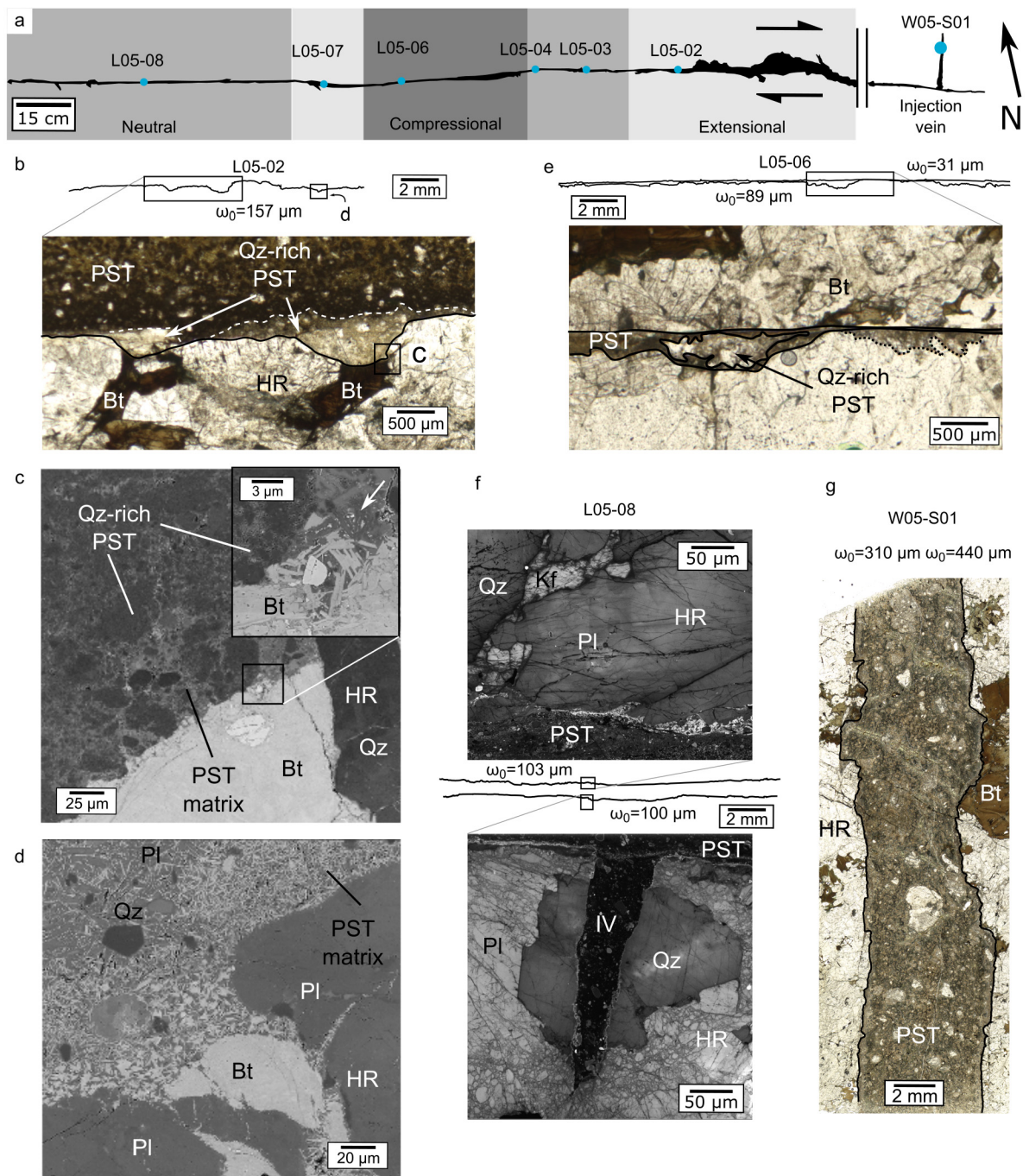


**Fig. 3.** Natural pseudotachyrites. (a) Drawing of the right lateral fault L05 (GPS point N46 10' 348" E10 34' 864") with sample location (blue dots). The compressional, neutral and extensional structural domains are evidenced by dark, intermediate and light gray-colored areas, respectively. (b) Southern pseudotachylyte-host rock (PST-HR) boundary from an extensional domain with two embayments on biotite grains (Bt). The embayments are partially filled by a whitish quartz-rich pseudotachylyte (sample L05-02). (c) Detail of the quartz-rich portion of the pseudotachylyte in (b). The PST is formed by abundant quartz clasts welded by devitrified glassy matrix and microlites of biotite and plagioclase (see also inset; white arrow = Pl microlites). This ultrafine aggregate is interpreted as a clast-laden melt filling the embayment. (d) Typical embayment in biotite at the PST-HR boundary (see profile in Fig. 3b for location). The PST matrix at the contact with the biotite grain includes microlites of biotite crystallized from the melt, indicative of progressive melting of the biotite grain followed by crystallization of biotite microlites during cooling and solidification of the melt. (e) Detail of the two PST-HR boundaries from a compressional domain. The northern boundary is smoother ( $\omega_0 = 31 \mu\text{m}$ ) than the southern one ( $\omega_0 = 89 \mu\text{m}$ ) (sample L05-06). (f) Host rocks located to the north (top, poorly damaged) and south (bottom, highly damaged) boundary of a neutral domain (sample L05-08). (g) PST-HR boundaries of an injection vein (sample W05-S01). IV, injection vein; Qz, quartz; Kf, K-feldspar; Pl, Plagioclase). (3b,e,g: Micro-images collected with polarized petrographic microscope, plane polarized light; 3c,d: FESEM-BSE images; 3f: FESEM-CL images).

the PST-HR boundary height) and  $\lambda_{ave}$  (average asperity radius), defined as:

$$\omega_0 = \sqrt{\frac{\sum_{i=1}^N z_i^2}{N}} \quad (1)$$

$$\lambda_{ave} = \sum_{i=1}^N \frac{\lambda_i}{N} \quad (2)$$

where  $z_i$  is the height of every point  $i$  of the PST-HR boundary with respect to  $z = 0$ , defined so that  $\sum_{i=1}^N z_i = 0$  (with  $N$  the number of points along the boundary);  $\lambda_i$  are the radii of the

**Table 2**

Electron microprobe analysis (EMPA) of experimental pseudotachylytes: (s.d. = standard deviation). Plagioclase and biotite compositions are from Di Toro and Pennacchioni (2004) and were obtained with the same electron microprobe and working conditions.

	PST matrix (Ca-rich)		PST matrix (Fe-rich)		Plagioclase <sup>a</sup>		Biotite <sup>a</sup>	
	6 data	s.d.	2 data	s.d.	15 data	s.d.	12 data	s.d.
SiO <sub>2</sub>	52.21	0.39	37.58		56.20	1.28	35.45	0.19
TiO <sub>2</sub>	1.16	0.07	2.73		0.02	0.01	2.55	0.50
Al <sub>2</sub> O <sub>3</sub>	22.11	0.30	17.82		26.96	0.94	17.33	0.20
FeO <sub>tot</sub>	7.71	0.27	21.53		0.38	0.29	20.59	0.42
MnO	0.26	0.04	0.59		0.12	0.11	0.01	0.01
MgO	3.92	0.20	9.73		0.02	0.01	9.04	0.46
CaO	4.84	0.19	0.08		9.33	1.02	0.03	0.04
Na <sub>2</sub> O	2.88	0.18	0.62		5.98	0.62	0.08	0.02
K <sub>2</sub> O	4.18	0.14	8.27		0.53	0.22	9.33	0.44
Tot	99.26	0.11	98.94		99.54	0.76	94.43	0.88

<sup>a</sup> Data from Di Toro and Pennacchioni (2004).

circles that approximate the curvature of the surface boundary around the maxima of the topography (e.g., embayments) calculated from finite differences at points  $i-1$ ,  $i$ ,  $i+1$  (Nielsen et al., 2010) (Fig. 1). The roughness of the PST-HR boundary is described by a series of continuous trigonometric functions where, for each function, the maximum amplitude  $z_i$  is  $\sqrt{2} \omega_0$  (Panzarasa and Tribulato, 1989) and the length  $\sqrt{2}\omega_0$  corresponds to the maximum depth of the embayments (Fig. 1). The MATLAB script, the thin section scans and the drawn PST-HR boundaries are available at <https://researchdata.cab.unipd.it/id/eprint/725> and in Supplementary Materials SM2.

### 3. Results

#### 3.1. Experimental pseudotachylytes

In S422, S423 and S475 experiments,  $\tau$  decreased from a peak value at initiation of slip towards an approximately constant residual value (called “steady-state” shear stress,  $\tau_{ss}$ ) of 2.70 MPa (at 20 MPa normal stress), 3.92 MPa (at 30 MPa) and 3.44 MPa (40 MPa) (Fig. 2a). These  $\tau_{ss}$  correspond to  $\dot{Q}_{ss}$  ( $\tau_{ss} V_{eq,ss}$  with  $V_{eq,ss} = 6.5 \text{ m s}^{-1}$ ; Fig. 2b) of 17.55, 25.50 and 22.36 MW m<sup>-2</sup>, respectively (Table 1). HRV376 experiment, performed at 1.3 m s<sup>-1</sup>, had  $\tau_{ss} = 3.86 \text{ MPa}$  (Di Toro et al., 2006) that correspond to  $\dot{Q}_{ss} = 5.02 \text{ MW m}^{-2}$ . In all the experiments, the PST-HR boundary is similar on both sides of the slip zone, with embayments at HR biotite grains (Fig. 2c). The experimental pseudotachylyte consists of abundant angularly shaped quartz clasts and few rounded plagioclase clasts immersed in a uniform gray in color or, in correspondence of biotite grains in the host rock, bright in color glassy-like matrix (BSE-SEM images, Fig. 2d-e). Biotite clasts were not found in the pseudotachylyte matrix. The most common gray in color matrix (“Ca-rich”) is enriched in Ti, Fe, Mn, Mg, and K and depleted in Si, Al, Ca and Na compared to the composition of plagioclase (the reverse is true of the composition of biotite) (Table 2). The less common bright in color matrix (“Fe-rich”) is found next to the biotite grains in the wall rocks and has a composition very similar to that of biotite (Table 2).

#### 3.2. Natural pseudotachylytes

In many individual faults of the Gole Larghe Fault Zone, the pseudotachylytes overprint cataclases with sub-greenschists facies assemblage made of quartz, plagioclase and K-feldspar clasts within a chlorite-epidote-rich matrix (Di Toro and Pennacchioni, 2005; Supplementary Materials SM3). Only pseudotachylyte-bearing fault segments across non-altered tonalite free of a precursor cataclase (Di Toro et al., 2006; Pittarello et al., 2008; Griffith et al., 2010) are considered here (Fig. 3). In pseudotachylyte fault veins, the PST-HR boundary shows embayments at biotite grains

(Fig. 3b-d) and at preexisting microcracks and (pressure) dissolution seams in the wall rock (Supplementary Materials SM3). Some embayments are filled by a quartz-rich portion of the pseudotachylyte formed by abundant quartz clasts welded by devitrified glassy matrix and microlites of biotite and plagioclase (Fig. 3b-c and inset). This ultrafine aggregate is interpreted as a clast-laden melt filling the embayment. However, most embayments in biotite are filled by the pseudotachylyte matrix rich in biotite acicular microlites (Fig. 3d). With respect to the north-facing PST-HR boundary, the southern one commonly shows (1) higher roughness (Fig. 3e), (2) more numerous injection veins (Di Toro et al., 2005) and, (3) more extensive and scattered shattering of quartz and plagioclase grains (in contrast with discrete microcracks sub-parallel to the main fault in the northern block: Fig. 3f). In injection veins (Mode I cracks), the PST-HR boundaries are rougher than in fault veins (Fig. 3g).

#### 3.3. Grain-scale roughness of the pseudotachylyte-host rock (PST-HR) boundary

In experimental pseudotachylytes, the magnitude and the slope of the FFT spectra are unrelated to  $\dot{Q}_{ss}$  (Figs. 4a and c). Moreover,  $\lambda_{ave}$  has a weak inverse relation with  $\omega_0$  (Fig. 5a) and is unrelated to  $\dot{Q}_{ss}$  (Fig. 5c) and,  $\omega_0$  decreases with increasing  $\dot{Q}_{ss}$  (Fig. 5e, Table 3). This negative trend of  $\omega_0$  with  $\dot{Q}_{ss}$  is due to the high  $\omega_0$  values of the grain-scale roughness of the PST-HR boundary from experiment HRV376, which was performed with a much lower  $\dot{Q}_{ss}$  (5.02 MW m<sup>-2</sup>) than the other experiments (17.55–25.50 MW m<sup>-2</sup>) (Table 1). The  $\omega_0$  values plot along the FFT spectra of their respective PST-HR boundaries (Fig. 4a), as expected by geometrical argumentations (this is the case also for the spectra of the natural pseudotachylytes) (Beeler, 2023).

In natural pseudotachylytes, the magnitude of the FFT spectra is higher in injection veins and extensional domains, and lower in neutral and compressional domains (Fig. 4b), the slopes of the FFT spectra are unrelated to the structural domain (Fig. 4d). The  $\lambda_{ave}$  has a weak inverse relation with  $\omega_0$  (Fig. 5b) and is unrelated to the structural domain (Fig. 5d) (Table 3). The value of  $\omega_0$  is higher in the injection veins than in the other structural domains with the lowest value measured in a compressional domain (L05-06N) (Fig. 5f).

### 4. Discussion

We first discuss the geometry of the PST-HR boundary in both experimental and natural pseudotachylytes. Then, by using the grain-scale roughness as correlating factor, we estimate  $\dot{Q}$  from the samples collected in fault L05 that cuts non-altered tonalite. In fact, PST-HR boundaries from natural faults with preexisting mi-

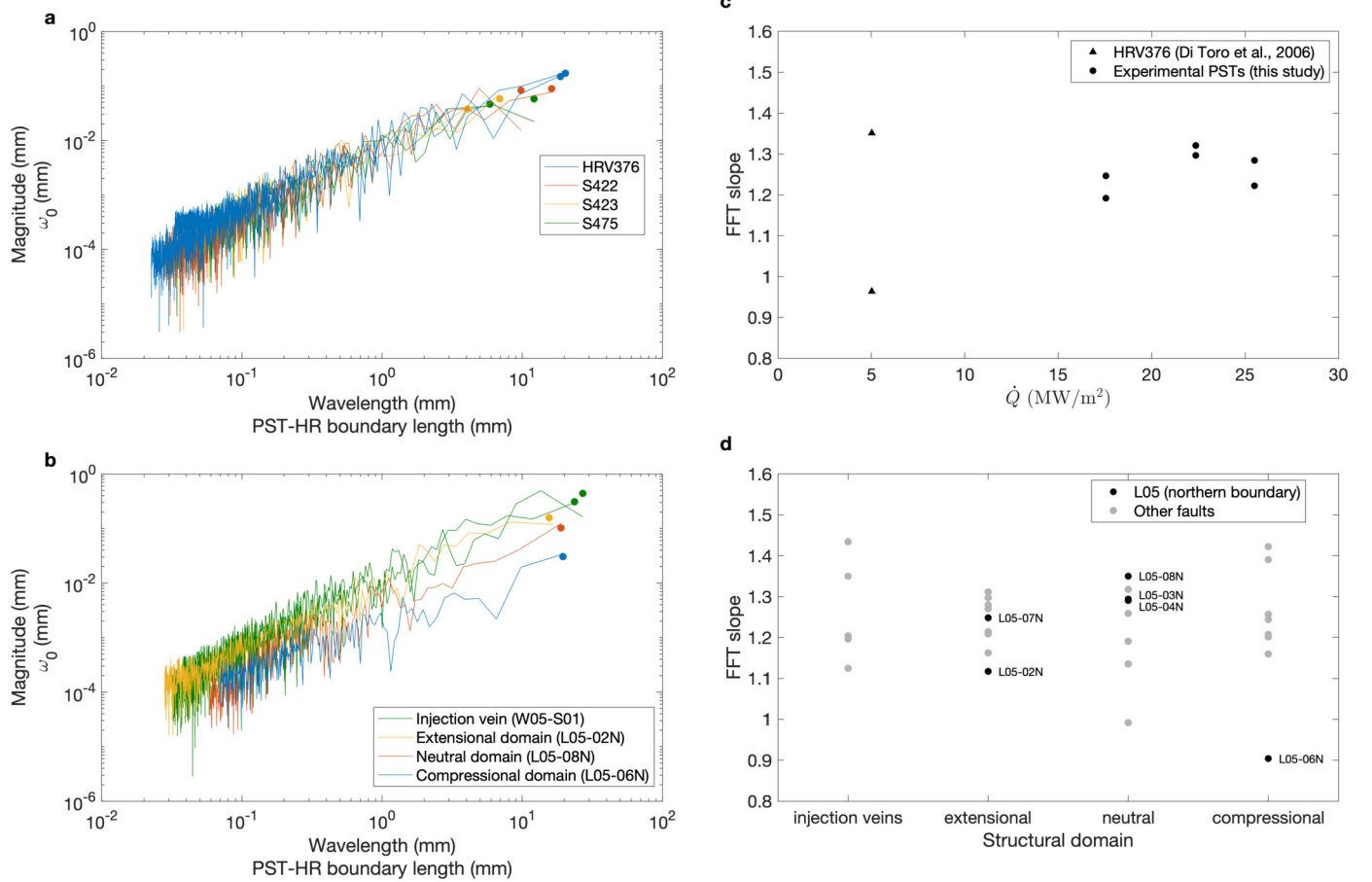


**Fig. 4.** Results of the Fast Fourier Transform (FFT) spectral analysis in experimental and natural pseudotachylytes. **(a)** FFT spectra of the experimental PST-HR boundaries (colored lines) with their respective  $\omega_0$  (= RMS, colored dots) vs. PST-HR boundary length. The  $\omega_0$  values plot along the FFT spectra of their respective PST-HR boundaries (Beeler, 2023). There are no substantial differences between the spectra of the four experimental pseudotachylytes. **(b)** Natural faults: FFT spectra of natural PST-HR boundaries (colored lines) with their respective  $\omega_0$  (= RMS, colored dots). For displaying purposes, only one spectrum from each structural domain is reported (See Supplementary Material SM2 for the entire dataset). The  $\omega_0$  values plot along the FFT spectra of their respective PST-HR boundaries. The FFT magnitude is higher in injection veins and extensional domain and lower in neutral and compressional domains. **(c)** Slope of the FFT spectra regression line of experimental PST-HR boundaries. There is no significant variation of the slope with increasing dissipated power. **(d)** Slope of the FFT spectra regression line of natural PST-HR boundaries of this study. As for the experiments, there is no clear correlation between the slopes and the structural domains. The stress normal to the fault increases from extensional to compressive structural domains. Hence, in natural faults,  $\dot{Q}_{ss}$  should also increase toward the right on the x-axis (see discussion).

crocracks and dissolution seams in their wall rocks were excluded from the analysis (see Supplementary Materials SM3).

Experimental pseudotachylytes were produced by sliding pre-cut cylinders. Therefore, the large stress perturbations expected during propagation of the seismic rupture tip in natural faults (e.g., Reches and Dewers, 2005) can be assumed negligible. We assume that the grain-scale roughness of experimental pseudotachylytes is mainly related to preferential melting of biotite. Once “steady-state” slip conditions are achieved in the experiment (Fig. 2a), the isotherms are approximately fixed in space (Nielsen et al., 2008). As a consequence, the solid rock specimen (1) passes through the isotherms during sample rotation, (2) heats up, (3) melts, (4) the melt is expelled because of the applied normal stress and centrifugal forces, and (5) the sample shortens at a constant rate (Nielsen et al., 2008) (Fig. 1). Under “steady-state” conditions the temperature  $T_z$  in the host rocks can be calculated by combining Eq. 4 and Eq. 70 in Nielsen et al. (2008):

$$T_z = (T_{melt} - T_i) \exp\left(-\frac{\tau \dot{u}}{\kappa \rho (L + c(T_m - T_i))}\right) + T_i. \quad (3)$$

By looking at the exponential in Eq. (3), for a given isotherm  $T_z$ , the thermal gradient in the host rocks perpendicular to the fault increases with increasing  $\dot{Q}$  ( $= \tau \dot{u}$ ). The formation of em-

bayments is controlled by preferential melting of biotite (Fig. 1). In the experiments the following parameters apply: melt temperature  $T_{melt} = 1450^\circ\text{C}$ ; rock density  $\rho = 2600 \text{ kg/m}^3$ ; latent heat  $L = 3.32 \times 10^5 \text{ J/kg}$  (Di Toro and Pennacchioni, 2004); ambient temperature  $T_i = 20^\circ\text{C}$ ; thermal diffusivity  $\kappa = 5 \times 10^{-7} \text{ m}^2/\text{s}$  for the temperature range 650–1450 °C of host rock melting (considering the nominal melting temperature of biotite as the lower end and the melt temperature as the higher end of this temperature range; Whittington et al., 2009); and specific heat capacity  $c = 1500 \text{ J/kg/K}$  (Waples and Waples, 2004).

In the experiments presented here, the temperature in the slip zone during frictional sliding was not measured because of technical limitations of the most used techniques (e.g., high speed infrared camera or thermocouples, see discussion in Aretusini et al., 2021). However, the estimated melt temperature of 1450 °C is consistent with the microstructural observations (Fig. 2d-e) and with the chemical composition of the pseudotachylyte glass (Table 2). In fact, (1) though the host rock tonalite is made by 49% plagioclase ( $An_{45}$ ), 29% quartz, 16% biotite and 6% K-feldspar, the clasts that survived from melting are mostly made of quartz (melting point 1730 °C), while there are few plagioclase  $An_{45}$  clasts (melting point 1250 °C, Spray, 2010; Deer et al., 1992) and none of biotite (Fig. 2d) and (2) melting of biotite and plagioclase melting largely contributes to the formation of the friction melt (see rounding of

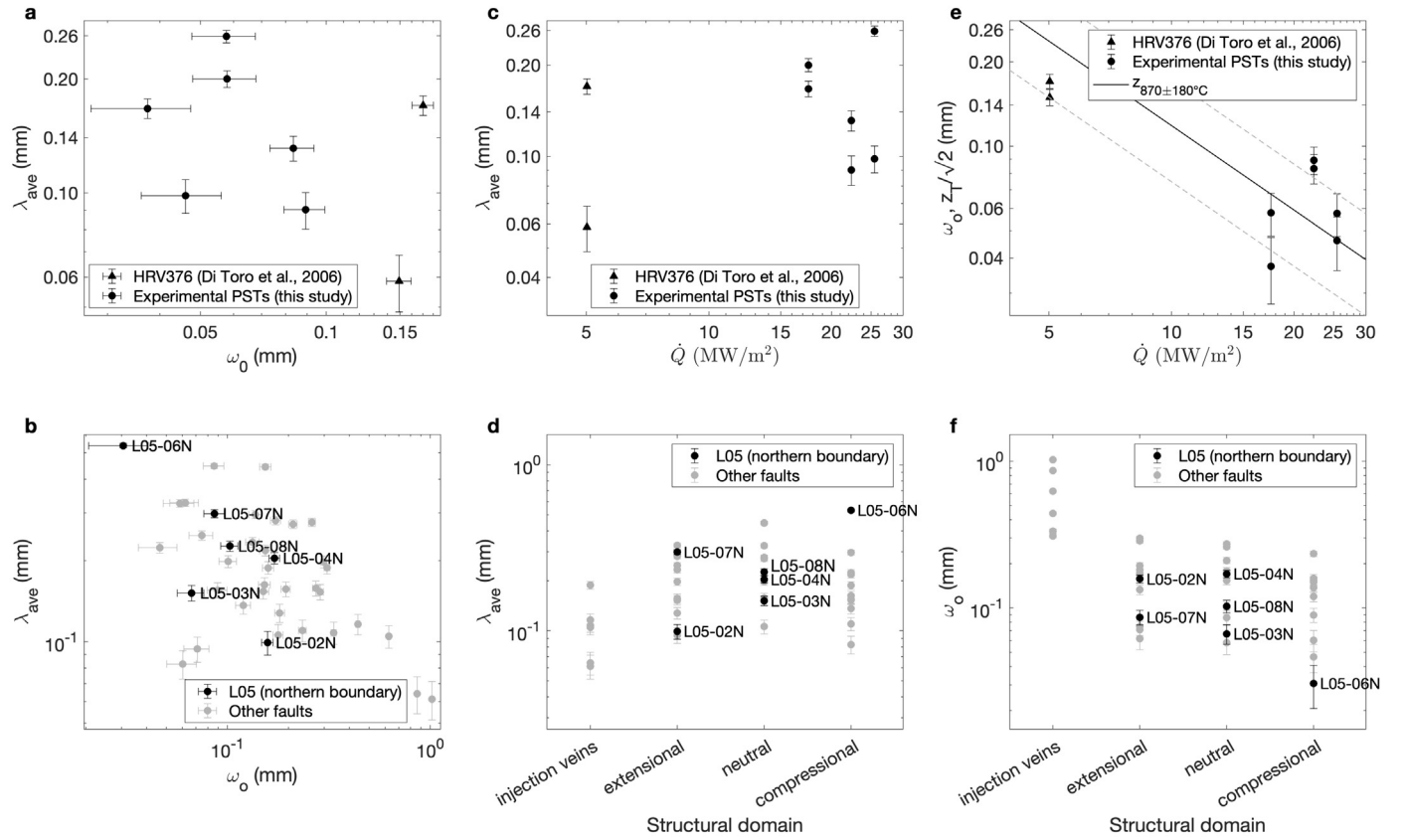


**Fig. 5.** Grain-scale roughness of the PST-HR boundary in experimental and natural pseudotachylytes (see Fig. 1 and Eqs. (1) and (2) for definition of  $\omega_0$  and  $\lambda_{ave}$ ). Sample locations and structural domains of the natural pseudotachylytes from the northern PST-HR fault L05 (black circles, see also discussion about these highlighted data) are reported in Fig. 3a. (a)  $\lambda_{ave}$  vs.  $\omega_0$  in experimental pseudotachylytes. (b)  $\lambda_{ave}$  versus  $\omega_0$  in natural pseudotachylytes. (c)  $\lambda_{ave}$  as function of  $\dot{Q}_{ss}$  in experimental pseudotachylytes. (d)  $\lambda_{ave}$  plotted for different structural domains in natural pseudotachylytes from this study. (e)  $\omega_0$  as function of  $\dot{Q}_{ss}$  in experimental pseudotachylytes. The solid black line is the distance  $z_{T=870^\circ\text{C}}/\sqrt{2}$ .  $T = 870^\circ\text{C}$  corresponds to the calculated melting temperature  $T_{m\text{eff}}$  for biotite, derived from the depth of the embayments (see discussion); gray in color dashed lines denote the standard deviation. The values of experimental  $\dot{Q}_{ss}$  are reported in Table 1. (f)  $\omega_0$  estimates for injection veins and for the different structural domains of fault veins in natural pseudotachylytes from this study.

plagioclase grains and incipient melting of biotite in Figs. 2d-e). This interpretation is supported by the elemental composition of the glassy matrix which has a  $\text{SiO}_2$  concentration slightly lower than the one of plagioclase but higher than that of biotite and by the presence of FeO,  $\text{K}_2\text{O}$ , CaO, MgO, etc. which is consistent with selective melting of plagioclase and biotite (and probably K-feldspar) (Table 2). We infer that the frictional melt temperature was larger than the melting point of plagioclase ( $1250^\circ\text{C}$  estimated from the solidus of plagioclase melting  $T$  at ambient pressure for  $\text{An}_{45}$  content, see Deer et al., 1992 and references therein) but lower than that of quartz ( $1730^\circ\text{C}$ , Navrotsky, 1995). The above temperature estimates, in the range of  $1450^\circ\text{C}$  and constrained by microstructural observations and geochemical investigations, are in the range of temperature estimates obtained from numerical models (Supplementary Materials SM1). The temperature increase in the slip zone due to shear heating was estimated using Finite Element Analysis to solve time dependent thermal diffusion in 2 dimensions (Cornelio et al., 2019). In the model, the heat source is the measured  $\tau(t) V_{eq}(t)$  and it is assumed that all the mechanical energy is dissipated as heat, a condition that appears to be satisfied in this experimental configuration (Niemeijer et al., 2011; Aretusini et al., 2021). According to numerical modeling results, temperatures of at least  $1450^\circ\text{C}$  were reached in all experiments, and for longer times in experiments performed with higher  $\dot{Q}_{ss}$  (Fig. SM1).

Lastly, we introduce  $z = \sqrt{2} \omega_0$ , with  $\omega_0$  calculated for each experimental PST-HR boundary. The length  $\sqrt{2} \omega_0$  is the distance of the bottom of the embayments from the reference plane  $z = 0$

and should correspond to the maximum penetration depth of the isotherm responsible for biotite melting (Fig. 1). Therefore, from Eq. (3), the effective melting temperature of biotite is  $T_{m\text{eff}} = 870^\circ\text{C} \pm 180^\circ\text{C}$ . This  $T_{m\text{eff}}$  is higher than the value  $T_m = 650^\circ\text{C}$  reported in the literature (Navrotsky, 1995). There are several possible explanations for this discrepancy. One is that because of kinetics effects, during the short time of the coseismic frictional heat pulse, biotite is not melted down to its nominal melting temperature  $T_m$ , but to a higher temperature  $T_{m\text{eff}}$ . A second explanation is related to the tribo-mechanical processes responsible for the formation and evolution of grain-scale roughness. For instance, (1) frictional melting may include more complex poly-phase quasi-equilibrium melting processes at the asperity scale (Lee et al., 2017) or, (2) the higher asperities made of quartz or feldspar may undergo continuous frictional wear, particularly where the friction melt is freely extruded and melt layer is thus thin. These two tribo-mechanical processes contribute to smoothing the grain-scale roughness by melting or wearing out those minerals that have a higher individual melting point than biotite. Therefore, the assumption that the grain-scale roughness of experimental pseudotachylytes is related only to preferential melting of biotite at  $T_m = 650^\circ\text{C}$  should be relaxed to include other micro-scale processes. In any case, the contribution of these second-order tribo-mechanical processes in defining the grain-scale roughness does not substantially alter the outcomes of our analysis as discussed below.

In natural pseudotachylyte-bearing faults, the extensional, neutral and compressional structural domains should correspond to

**Table 3**  
Grain-scale roughness parameters of the experimental and natural samples analyzed in this study.

Sample	$\lambda_{ave}$ (mm)	$\lambda_{ave}$ deviation (mm)	$\omega_0$ (mm)	$\omega_0$ deviation (mm)	FFT slope (adimen.)	FFT intercept (mm)	$\dot{Q}_{ss}$ or structural domain ( $\text{MW m}^{-2}$ )
HRV376 top	0.1702	0.1714	0.1703	0.1768	0.9639	-5.2620	5.020
HRV376 bot	0.0586	0.0511	0.1493	0.1463	1.3516	-4.5176	5.020
S422 top	0.1312	0.1540	0.0833	0.0772	1.3211	-4.6116	22.36
S422 bot	0.0903	0.0796	0.0892	0.0865	1.2966	-5.1414	22.36
S423 top	0.1671	0.1398	0.0374	0.0341	1.2463	-4.7004	17.55
S423 bot	0.2000	0.2039	0.0579	0.0578	1.1918	-5.2449	17.55
S475 top	0.0983	0.0538	0.0461	0.0481	1.2846	-4.7907	25.50
S475 bot	0.2590	0.2705	0.0577	0.0606	1.2220	-5.1841	25.50
A1E	0.1047	0.1319	0.6252	0.6059	1.4345	-3.7856	injection vein
A1W	0.1080	0.1357	0.3346	0.3595	1.2042	-4.3912	injection vein
A02-02N	0.2474	0.2072	0.0747	0.0797	1.2144	-5.4969	neutral
A02-02S	0.0941	0.0999	0.0710	0.0702	1.2975	-4.4707	neutral
A02-04N	0.1364	0.1522	0.1197	0.1156	1.2074	-5.2784	compressional
A2E	0.0642	0.0641	0.8621	0.8853	1.1964	-4.4267	injection vein
A2W	0.0613	0.0831	1.0217	1.0851	1.3500	-4.5118	injection vein
A4N	0.2769	0.2175	0.2613	0.2588	1.3176	-5.5750	neutral
A4S	0.1578	0.1396	0.2729	0.2554	1.1910	-4.9211	neutral
A5N	0.1277	0.1259	0.1812	0.1848	1.2490	-5.4868	extensional
A5S	0.2333	0.2149	0.1331	0.1431	1.2801	-5.2390	extensional
A7N	0.1625	0.1625	0.1525	0.1396	1.2450	-5.4098	compressional
A7S	0.2957	0.1966	0.1374	0.1376	1.2016	-5.5869	compressional
L05-02N	0.0992	0.1138	0.1577	0.1601	1.1171	-4.8767	extensional
L05-03N	0.1515	0.1470	0.0666	0.0643	1.2943	-5.0969	neutral
L05-04N	0.2039	0.2184	0.1707	0.1552	1.2910	-5.0811	neutral
L05-04S	0.1059	0.1073	0.1780	0.1750	1.2922	-4.3669	neutral
L05-06N	0.5323	0.2699	0.0307	0.0341	0.9041	-6.3854	compressional
L05-06S	0.1553	0.2183	0.0895	0.0773	1.1598	-5.1893	compressional
L05-07N	0.2979	0.2356	0.0864	0.0816	1.2482	-4.8399	extensional
L05-07S	0.3271	0.2671	0.0619	0.0584	1.1624	-4.6570	extensional
L05-08N	0.2260	0.1991	0.1027	0.0955	1.3502	-5.4975	neutral
L05-08S	0.1982	0.1682	0.1008	0.0945	1.2591	-5.6017	neutral
L09-01aN	0.1527	0.1740	0.2870	0.2872	1.2703	-4.9312	extensional
L09-01aS	0.1974	0.1759	0.2986	0.3298	1.2092	-4.9801	extensional
L09-02aN	0.1877	0.1522	0.1589	0.1578	1.2573	-5.1675	compressional
L09-02aS	0.2178	0.2046	0.1540	0.1408	1.2445	-5.3854	compressional
L09-02bN	0.2230	0.2191	0.0464	0.0429	1.1145	-5.9520	compressional
L09-02bS	0.0827	0.0883	0.0602	0.0544	1.2487	-4.8847	compressional
L09-03aN	0.2723	0.3508	0.2109	0.1974	1.1890	-5.6802	neutral
L09-03aS	0.4446	0.2220	0.1541	0.1720	0.9918	-5.5594	neutral
L09-03bN	0.3253	0.2289	0.0582	0.0554	1.1462	-5.5622	neutral
L09-03bS	0.4476	0.4125	0.0859	0.0798	1.1353	-5.0145	neutral
W05-S01E	0.1162	0.1509	0.4403	0.4540	1.3453	-4.6167	injection vein
W05-S01W	0.1882	0.1789	0.3100	0.2837	1.1248	-4.3834	injection vein
W05-S04N	0.1565	0.1735	0.1941	0.1963	1.2653	-5.5436	extensional
W05-S04S	0.2812	0.2011	0.1728	0.1752	1.3115	-4.5132	extensional
W09-S01N	0.1100	0.1293	0.2344	0.2318	1.3903	-4.8358	compressional
W09-S01S	0.1537	0.1201	0.1502	0.1541	1.4221	-5.1237	compressional

domains of low, intermediate and high normal (effective) stresses  $\sigma_n$ , respectively. The nearby domains of fault L05 (Fig. 3a) should have recorded a similar slip history under comparable average co-seismic slip rates (Griffith et al., 2010). When the fault is lubricated by friction melts, the frictional traction  $\tau$  and, therefore,  $\dot{Q}$  are expected to be higher in the compressional structural domains ( $\tau \propto \sigma_n^{0.25}$ , Nielsen et al., 2008) than in neutral and extensional ones. In the case of injection veins (mode I cracks) the frictional traction is negligible and the PST-HR boundary should be mainly affected by fracturing and by melt-rock interaction. In fact, in injection veins the melt temperature is independent of the frictional power (here,  $\dot{Q} = 0$ ) and, the melt, once injected, cools slowly to ambient temperature as the melting front propagates in the wall rocks (“Stefan problem”, Ch. XI in Carslaw and Jaeger, 1959). This type of melt-rock interaction results in a lower temperature gradient in the wall rocks and in a higher grain-scale roughness at the PST-HR boundary. Consistent with this interpretation, the  $\omega_0$  values are systematically higher in injection veins than in fault veins (Fig. 5f). In fault veins, the grain-scale roughness of the PST-HR boundary is affected by:

1. Asymmetric and intense damage associated with the transient stress perturbation during the propagation of the seismic rupture front at some  $\text{km s}^{-1}$  (Poliakov et al., 2002). For eastward propagating ruptures of the Gole Larghe right-lateral strike slip faults, stress perturbation induced intense fracturing and wall-rock spallation especially in the southern block of individual faults (Di Toro et al., 2005) (Fig. 3f bottom). In contrast, the orientation of the microcracks in the northern wall rock is sub-parallel to the E-W strike of the fault (Fig. 3f top). This orientation is consistent with the direction of the maximum transient compressive stress associated with eastward rupture propagation along a right-lateral strike slip fault (Fig. 4 in Di Toro et al., 2005). According to this interpretation, the northern and southern blocks were located on the transient compression and tension stress fields, respectively, of the ancient rupture that propagated along this fault segment. The grain-scale roughness resulting from the stress perturbation at the rupture-tip is not included in the theoretical model which relates the grain-scale roughness to  $\dot{Q}$  (Nielsen et al., 2010);
2. Reworking of the PST-HR boundary due, for instance, to filling of embayments by the clasts carried by the melt (Figs. 3b-c).



The resulting grain-scale roughness should be excluded from our analysis (see black in color line in Fig. 3b).

3. Preferential melting of biotite with respect to the other host rock-forming minerals due to non-equilibrium frictional melting. This would result in the grain-scale roughness related to the  $\dot{Q}$  in the process zone that is considered in the theoretical analysis by Nielsen et al. (2010). We note here that grain-scale roughness will thus reflect not only the heating rate of the slipping zone and the associated thermal gradient in the wall rocks but also the relative melting points of the various mineral phases and their grain sizes. We make also the assumption that steady-state conditions during frictional melting were achieved. This assumption might be partly relaxed by the evidence that in the selected natural faults the pseudotachylite matrix at the contact with the biotite grains in the wall rock includes biotite microlites precipitated from the melt (Fig. 3d). In addition, the embayments are laterally confined by well-rounded plagioclase grains (Fig. 3d). The above microstructural evidence is consistent with progressive migration of the isotherms and associated melting front in the wall rock tonalite (Fig. 1), followed by crystallization of biotite microlites during cooling and solidification of the melt (Fig. 3d).

Based on the above analysis of the physical processes that shape the PST-HR boundary, we decided to use  $\omega_0$  to estimate  $\dot{Q}$  within the several parameters (magnitude and slope of FFT,  $\omega_0$  and  $\lambda_{ave}$ ) that describe the grain-scale roughness (Table 3). In fact, the FFT magnitude of the PST-HR boundary is affected by  $\dot{Q}$  only in the natural pseudotachylites (Figs. 4a-b). Instead, the slope of the FFT is a measure of roughness scaling across the scale of measurements (10  $\mu\text{m}$  – 10's of mm) and thus is not necessarily affected by  $\dot{Q}$  (Beeler, 2023). Moreover, there is not a clear dependence of  $\lambda_{ave}$  with  $\dot{Q}$  or the structural domain (Figs. 5c-d). In fact, while the value of  $\omega_0$  represents the roughness at the profile scale (6.7–34.5 mm) spanning ~3-17 grains and may thus be particularly sensitive to grain-scale roughness,  $\lambda_{ave}$  is a local measure comparing neighboring profile points (across 30  $\mu\text{m}$ ), which is much smaller than the grain scale. The poor dependence of  $\lambda_{ave}$  with  $\dot{Q}$  is due to the fact that melting along sliding surfaces is the primary driver of the grain-scale roughness, and, consequently,  $\lambda_{ave}$  depends on both grain size and melting point of the individual minerals. Since the tonalites discussed here that host the natural and experimental pseudotachylite have the same average grain size,  $\lambda_{ave}$  is poorly dependent of  $\dot{Q}$ . In contrast,  $\omega_0$ , although like  $\lambda_{ave}$  varies with grain size and melting point of the host rock minerals (e.g., the maximum value of  $\omega_0$  will be limited by the size of the mineral with the lowest melting point), it depends also on the heating rate of the slipping zone and the associated thermal gradient in the wall rocks, which are proportional to  $\dot{Q}$  (Fig. 1).

Because of the effect of the processes listed at points 1 and 2 above, to estimate  $\dot{Q}$  we consider the northern PST-HR boundary of the samples from fault L05. In these pseudotachylites, (1) there is no evidence for sub-greenschists facies cataclastic precursors (Fig. 3), and (2) the northern block was less affected by the coseismic stress perturbation because located in the compression field of the eastward propagating rupture (Fig. 3f, see Di Toro et al., 2005). We can reasonably assume that in these samples the grain-scale roughness is mainly related to the preferential melting of biotite (Fig. 3d). From the analysis of the experimental pseudotachylites the calculated melting temperature for biotite is assumed to be  $T_{meff} = 870^\circ\text{C}$  (Fig. 5e); substituting it as  $T_z$  in Eq. (3) and rearranging the equation we obtain:

$$\tau \dot{u} = \frac{\kappa \rho (L + c (T_m - T_i))}{\sqrt{2} \omega_0} \ln \left( \frac{T_m - T_i}{870^\circ\text{C} - T_i} \right) \quad (4)$$

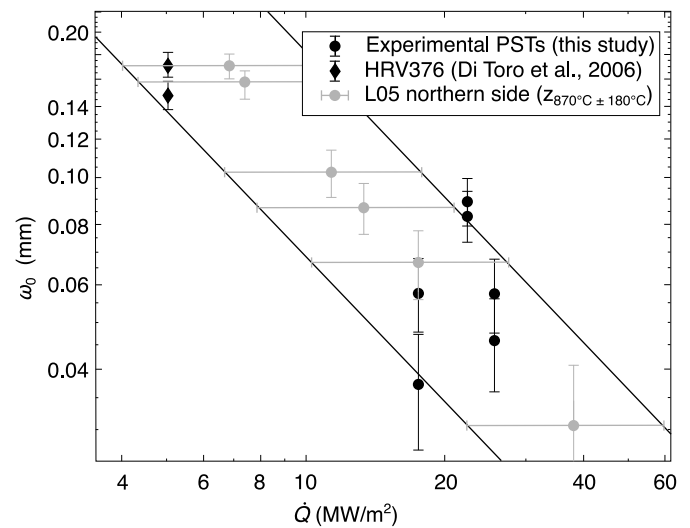


**Fig. 6.** Frictional power dissipation ( $\dot{Q}$ ) range estimated for the fault segment L05 using the grain-scale roughness of the northern pseudotachylite-host rock boundary (gray dots) together with the calculated frictional power dissipation derived from the experimental pseudotachylites of this study (black dots) and of Di Toro et al. (2006) (diamonds). The estimate is based on the melting temperature of biotite derived from the experimental pseudotachylites ( $870^\circ\text{C} \pm 180^\circ\text{C}$ , Fig. 5d).

where  $T_i = 250^\circ\text{C}$  is ambient temperature during seismic faulting (Di Toro and Pennacchioni, 2004). The estimated  $\dot{Q}$  ( $\tau \dot{u}$ ) for the natural pseudotachylites of the northern boundary of fault L05 are reported in Fig. 6. On this diagram, we also plot the  $\omega_0$  vs.  $\dot{Q}$  measurements for the experimental pseudotachylites. According to this analysis, natural pseudotachylites are the result of  $\dot{Q}$  ranging from 4 to 60  $\text{MW m}^{-2}$ , with an arithmetic mean value of 16  $\text{MW m}^{-2}$ .

These first  $\dot{Q}$  estimates obtained from field and microstructural observations are in the lower range of the broad  $\dot{Q}$  range from 3 to 300  $\text{MW m}^{-2}$  proposed in the literature (Fig. 2 in Sibson, 1980). But these latter estimates were based on a range of possible coseismic shear stress ( $30 < \tau < 300$  MPa) and on-fault slip rate ( $0.1 < \dot{u} < 1.0$  m/s) achieved at crustal seismicogenic depths of about 10 km (i.e., these hypocentral depths are about the same as in our study). The proposed  $\dot{Q}$  estimates of  $> 100$   $\text{MW m}^{-2}$  would have been excessive because they would have induced very high temperatures in the slip zone ( $> 10,000^\circ\text{C}$ ), unless a relevant reduction in  $\tau$  during coseismic slip was considered (see Fig 4 in Sibson, 1980). Though our field estimates of  $\dot{Q}$  (mean value 16  $\text{MW m}^{-2}$ ) were determined in a fault patch and may not be representative of the entire fault, they are supported by experimental evidence and are in agreement with the hypothesis by Sibson (1980) of large reduction in  $\tau$  during seismic slip (Fig. 2a). In addition, the estimates of  $\dot{Q}$  proposed here are based on microstructural observations associated with the effects of temperature increase in the slip zone (Figs. 1–3) rather than on approximate estimates of deformation conditions during coseismic slip.

## 5. Conclusions

What is the magnitude of the frictional power ( $\dot{Q}$ ) dissipated on a fault during an earthquake? We address this question by exploiting a theoretical model which relates the grain-scale roughness of the pseudotachylite-host rock boundary described by the characteristic asperity height  $\omega_0$  to  $\dot{Q}$  (Nielsen et al., 2010) (Fig. 1). In experimental pseudotachylites produced under known  $\dot{Q}$  (Fig. 2),  $\omega_0$  decreases with increasing  $\dot{Q}$  (Fig. 5e), as predicted by the model (Fig. 1). In natural pseudotachylites from the Gole Larghe Fault Zone within the Adamello tonalites,  $\omega_0$  is higher for

injection veins (where  $\dot{Q}$  should be negligible) than for extensional, neutral and compressional fault domains (Fig. 5f). These domains should correspond to low, intermediate and high  $\dot{Q}$ , respectively (Figs. 5e-f). Contrary to experimental pseudotachylytes, produced by shearing precut samples, the grain-scale roughness of natural pseudotachylyte PST-HR boundary is also affected by the intense damage associated with the propagation of the seismic rupture tip. In the Gole Larghe Fault Zone, this host rock damage is especially developed in the southern wall block. Therefore, to estimate  $\dot{Q}$  we considered six samples of the northern boundary of fault L05. In fact, the interpretation of the microstructures (Fig. 3) suggests that the grain-scale roughness of the northern side of fault L05 mainly resulted from preferential melting of biotite (Fig. 3d). From the experimental dataset we estimate with Eq. (3) the (effective) melting temperature  $T_{m\text{ eff}} = 870^\circ\text{C}$  of biotite during frictional melting. This estimate is based on the depth  $z = \sqrt{2} \omega_0$  of the embayments, which should correspond to the maximum penetration depth of the isotherm responsible for biotite melting. Finally, by inserting  $z = \sqrt{2} \omega_0$  in Eq. (4) for the samples from fault L05, we estimate  $\dot{Q}$  which ranges from 4 to 60  $\text{MW m}^{-2}$ , with an average value of 16  $\text{MW m}^{-2}$ . These  $\dot{Q}$  values are in the lower range of very broad estimates (3–300  $\text{MW m}^{-2}$ ) based on typical average seismic slip rates and frictional tractions inferred for the upper continental crust (Sibson, 1980). In addition, these low estimates of  $\dot{Q}$  would suggest that the pseudotachylytes studied, at least at the scale of the fault patch investigated (a few  $\text{m}^2$ ), may be representative of earthquakes that have excess radiated seismic energy (Beeler et al., 2016). Actually, our estimates of  $\dot{Q}$  based on field and microstructural observations, although valid for fault patches of few  $\text{m}^2$  in size, could be compared with  $\dot{Q}$  values obtained in the rare cases where absolute stress levels, and hence  $\tau(t) \dot{u}(t)$ , can be estimated (Spudich, 1992; Milliner et al., 2022). However, our field-based estimates of frictional power per unit area dissipated during earthquakes, although independent of assumptions about the magnitude of seismic slip rates and shear tractions, may suffer from a number of other assumptions as discussed above. For instance, the theoretical model does not include (1) non-steady-state conditions and second order effects (e.g., latent heat of melting, mineral and temperature-dependent thermal conductivity variations) which may perturb the curvature of the isotherms migrating in the wall rocks (i.e., we assumed planar isotherms in Fig. 1) or (2) other tribo-mechanical processes that may contribute to the shaping of the grain-scale roughness. Nevertheless, the approach presented here can be applied to pseudotachylytes produced in other geodynamic settings and at deeper crustal levels and will help determine this relevant but elusive parameter of the earthquake source.

### CRediT authorship contribution statement

**F. Lazari:** Conceptualization, Writing – Original Draft, Methodology, Software, Formal analysis, Investigation, Data Curation. **A. Castagna:** Conceptualization, Writing – Review & Editing, Methodology, Software, Formal analysis, Investigation, Data Curation. **S. Nielsen:** Conceptualization, Writing – Review & Editing, Software, Investigation, Resources, Funding acquisition. **A.W. Griffith:** Conceptualization, Writing – Review & Editing, Methodology, Software. **G. Pennacchioni:** Writing – Review & Editing, Investigation, Resources, Funding acquisition. **R. Gomila:** Methodology, Writing – Review & Editing, Resources. **P. Resor:** Writing – Review & Editing, Methodology, Investigation, Funding acquisition. **C. Cornelio:** Review & editing, thermal modeling. **G. Di Toro:** Conceptualization, Writing – Review & Editing, Methodology, Investigation, Resources, Supervision, Project administration, Funding acquisition.

### Declaration of competing interest

The authors declare that they have no known competing financial interests or personal relationships that could have appeared to influence the work reported in this paper.

### Data availability

All the data and the MATLAB script can be downloaded from: <https://researchdata.cab.unipd.it/id/eprint/725>.

### Acknowledgements

GDT and SN acknowledge the ERC StG USEMS (205175) and CoG NOFEAR (614705) projects, RG the European Union Marie Skłodowska-Curie project FRICTION (896346), GP and GDT the PRIN 2022 project THALES, and PR NSF EAR-1145238. Leonardo Tauro is thanked for thin section preparation. All authors thank Romano Ceschin from the Rifugio Ai Caduti dell'Adamello for his generous hospitality. Rebecca Bendick (EPSL Editor), Nicholas Beeler and an anonymous reviewer are thanked for their suggestions and constructive comments.

### Appendix A. Supplementary material

Supplementary material related to this article can be found online at <https://doi.org/10.1016/j.epsl.2023.118057>.

### References

- Andersen, T.B., Mair, K., Austrheim, A., Podladchikov, Y., Vrijmoed, J.C., 2008. Stress release in exhumed intermediate and deep earthquakes determined from ultramafic pseudotachylyte. *Geology* 36, 995–998.
- Aretusini, S., Núñez-Cascajero, A., Spagnuolo, E., Tapetado, A., Vázquez, C., Di Toro, G., 2021. Fast and localized temperature measurements during simulated earthquakes in carbonate rocks. *Geophys. Res. Lett.* 48, e2020GL091856. <https://doi.org/10.1029/2020GL091856>.
- Beeler, N., 2023. On the scale-dependence of fault surface roughness. *J. Geophys. Res.* <https://doi.org/10.1029/2022JB024856>.
- Beeler, N., Di Toro, G., Nielsen, S., 2016. Earthquake source properties from pseudotachylyte. *Bull. Seismol. Soc. Am.* 106, 2764–2776.
- Callegari, E., Brack, P., 2002. Geological map of the Tertiary Adamello batholith (Northern Italy) explanatory notes and legend. *Mem. Sci. Geol.* 54, 19–49.
- Carslaw, H.S., Jaeger, J.C., 1959. *Conduction of Heat in Solids*, 2nd edition. Oxford at the Clarendon Press, Oxford.
- Cornelio, C., Spagnuolo, E., Di Toro, G., Nielsen, S., Violay, M., 2019. Mechanical behaviour of fluid-lubricated faults. *Nat. Commun.*, 1–7. <https://doi.org/10.1038/s41467-019-09293-9>.
- Deer, W.A., Howie, R.A., Zussman, J., 1992. *An Introduction to Rock-Forming Minerals*, 2nd ed. Longman Scientific & Technical, Harlow (UK).
- Di Toro, G., Pennacchioni, G., 2004. Superheated friction-induced melts in zoned pseudotachylytes within the Adamello tonalites (Italian Southern Alps). *J. Struct. Geol.* 26 (10), 1783–1801.
- Di Toro, G., Pennacchioni, G., 2005. Fault plane processes and mesoscopic structure of a strong-type seismogenic fault in tonalites (Adamello batholith, Southern Alps). *Tectonophysics* 402, 55–80.
- Di Toro, G., Nielsen, S., Pennacchioni, G., 2005. Earthquake rupture dynamics frozen in exhumed ancient faults. *Nature* 436, 1009–1012.
- Di Toro, G., Hirose, T., Nielsen, S., Pennacchioni, G., Shimamoto, T., 2006. Natural and experimental evidence of melt lubrication of faults during earthquakes. *Science* 311, 647–649.
- Di Toro, G., Niemeijer, A., Tripoli, A., Nielsen, S., Di Felice, F., Scarlato, P., Spada, G., Alessandrini, R., Romeo, G., Di Stefano, G., Smith, S., Spagnuolo, E., Mariano, S., 2010. From field geology to earthquake simulation: a new state-of-the-art tool to investigate rock friction during the seismic cycle (SHIVA). *Rend. Lincei* 21, 95–114.
- Di Toro, G., Han, R., Hirose, T., De Paola, N., Nielsen, S., Mizoguchi, K., Ferri, F., Cocco, M., Shimamoto, T., 2011. Fault lubrication during earthquakes. *Nature* 471, 494–499.
- Ferrand, T.P., Nielsen, S., Labrousse, L., Schubnel, A., 2021. Scaling seismic fault thickness from the laboratory to the field. *J. Geophys. Res.* 126, e2020JB020694.
- Fialko, Y., Khazan, Y., 2005. Fusion by the earthquake fault friction: stick or slip? *J. Geophys. Res.* 110, B12407.

- Griffith, W.A., Nielsen, S., Di Toro, G., Smith, S.A.F., 2010. Rough faults, distributed weakening, and off-fault deformation. *J. Geophys. Res.* 115, B08409.
- Guatterri, M., Spudich, P., 1998. Coseismic temporal changes of slip direction: the effect of absolute stress on dynamic rupture. *Bull. Seismol. Soc. Am.* 88, 777–789.
- Hirose, T., Shimamoto, T., 2005. Slip-weakening distance of faults during frictional melting as inferred from experimental and natural pseudotachylytes. *Bull. Seismol. Soc. Am.* 95, 1666–1673.
- Hosseinzadehsabeti, E., Ferré, E.C., Andersen, T.B., Geissman, J.W., Bilardello, D., Di Toro, G., 2021. Focal mechanisms of intraslab earthquakes: insights from pseudotachylytes in mantle units. *J. Geophys. Res.*, e2020JB021479.
- Johnson, S.E., Song, W.J., Vel, S.S., Song, B.R., Gerbi, C.C., 2021. Energy partitioning, dynamic fragmentation, and off-fault damage in the earthquake source volume. *J. Geophys. Res.* 126, e2021JB022616.
- Lee, S.K., Han, R., Jeong, G.Y., Khim, H., Hirose, T., 2017. Quasi-equilibrium melting of quartzite upon extreme friction. *Nat. Geosci.* 10, 436–442.
- Maddock, R.H., Grocott, J., Van Nes, M., 1987. Vesicles, amygdalae and similar structures in fault-generated pseudotachylytes. *Lithos* 20, 419–432.
- Magloughlin, J.F., Spray, J.G., 1992. Frictional melting processes and products in geological materials: introduction and discussion. *Tectonophysics* 204, 197–206.
- Milliner, C.W.D., Aati, S., Avouac, J., 2022. Fault friction derived from fault bend influence on coseismic slip during the 2019 Ridgecrest Mw 7.1 mainshock. *J. Geophys. Res.* 127, e2022JB024519.
- Mitterpergher, S., Zanchi, A., Zanchetta, S., Fumagalli, M., Gukov, K., Bistacchi, A., 2021. Fault reactivation and propagation in the northern Adamello pluton: the structure and kinematics of a kilometre-scale seismogenic source. *Tectonophysics* 806, 228790.
- Navrotsky, A., 1995. Thermodynamic properties of minerals. In: *Rock Physics and Phase Relations. A Handbook of Physical Constants*. In: AGU Reference Shelf, vol. 2, pp. 18–32.
- Nielsen, S., Di Toro, G., Hirose, T., Shimamoto, T., 2008. Frictional melt and seismic slip. *J. Geophys. Res.* 113, B01308.
- Nielsen, S., Di Toro, G., Griffith, W.A., 2010. Friction and roughness of a melting rock surface. *Geophys. J. Int.* 182, 299–310.
- Nielsen, S., Spagnuolo, E., Violay, M., 2012. The ultimate sample preparation for rotary shear experiments. *Rapporti tecnici INGV*. <http://istituto.ingv.it/l-ingv/produzione-scientifica/rapporti-tecnici-ingv/numeri-pubblicati-2012S>.
- Niemeijer, A., Di Toro, G., Nielsen, S., Di Felice, F., 2011. Frictional melting of gabbro under extreme experimental conditions of normal stress, acceleration, and sliding velocity. *J. Geophys. Res.* 116, B07404.
- Panzarasa, G., Tribulato, S., 1989. Serie di funzioni. Edizioni Tecnos, Milano, p. 124.
- Papa, S., Pennacchioni, G., Ross, J.A., Faccenda, M., 2018. The fate of garnet during (deep-seated) coseismic frictional heating: the role of thermal shock. *Geology* 46, 471–474.
- Petley-Ragan, A., Ben-Zion, Y., Austrheim, H., Ildefonse, B., Renard, F., Jamtveit, B., 2019. Dynamic earthquake rupture in the lower crust. *Sci. Adv.* 5, eaaw0913.
- Pittarello, L., Di Toro, G., Bizzarri, A., Pennacchioni, G., Hadizadeh, J., Cocco, M., 2008. Energy partitioning during seismic slip in pseudotachylyte-bearing faults (Gole Larghe Fault, Adamello, Italy). *Earth Planet. Sci. Lett.* 269, 131–139.
- Poliakov, A.N.B., Dmowska, R., Rice, J.R., 2002. Dynamic shear rupture interactions with fault bends and off-axis secondary faulting. *J. Geophys. Res.* 107 (B11), 2295.
- Pozzi, G., De Paola, N., Nielsen, S.B., Holdsworth, R.E., Tesei, T., Thieme, M., Demouchy, S., 2021. Coseismic fault lubrication by viscous deformation. *Nat. Geosci.* 14, 437–442.
- Reches, Z., Dewers, T.A., 2005. Gouge formation by dynamic pulverization during earthquake rupture. *Earth Planet. Sci. Lett.* 235, 361–374.
- Rice, J.R., 2006. Heating and weakening of faults during earthquake slip. *J. Geophys. Res.* 111, B05311.
- Shand, S.J., 1916. The pseudotachylyte of Parijs (Orange Free State) and its relation to "trap-shotten gneiss" and "flinty crush rock". *Q. J. Geol. Soc. Lond.* 72, 198–221.
- Sibson, R.H., 1975. Generation of pseudotachylyte by ancient seismic faulting. *Geophys. J. R. Astron. Soc.* 43, 775–794.
- Sibson, R.H., 1980. Power dissipation and stress levels on faults in the upper crust. *J. Geophys. Res.* 85, 6239–6247.
- Sibson, R.H., 2003. Thickness of the seismic slip zone. *Bull. Seismol. Soc. Am.* 93, 1169–1178.
- Smith, S.A.F., Bistacchi, A., Mitchell, T.M., Mitterpergher, S., Di Toro, G., 2013. The structure of an exhumed intraplate seismogenic fault in crystalline basement. *Tectonophysics* 599, 29–44.
- Spray, J.G., 1995. Pseudotachylyte controversy: fact or friction? *Geology* 23, 1119–1122.
- Spray, J.G., 2010. Frictional melting processes in planetary materials: from hypervelocity impact to earthquakes'. *Annu. Rev. Earth Planet. Sci.* 38, 221–254.
- Spudich, P., 1992. On the inference of absolute stress levels from seismic radiation. *Tectonophysics* 211, 99–106.
- Swanson, M.T., 1992. Fault structure, wear mechanisms and rupture processes in pseudotachylyte generation. *Tectonophysics* 204, 223–242.
- Tullis, T.E., 2015. Mechanisms for friction of rock at earthquake slip rates. In: Kanamori, H. (Ed.), *Treatise on Geophysics*, vol. 4, 2nd edition. Elsevier, pp. 139–159.
- Udias, A., Madariaga, R., Buforn, E., 2014. *Source Mechanism of Earthquakes: Theory and Practice*. Cambridge University Press.
- Waples, D.W., Waples, J.S., 2004. A review and evaluation of specific heat capacities of rocks, minerals, and subsurface fluids. Part 1: minerals and nonporous rocks. *Nat. Resour. Res.* 13, 97–122.
- Whittington, A.G., Hofmeister, A.M., Nabelek, P.I., 2009. Temperature-dependent thermal diffusivity of the Earth's crust and implications for magmatism. *Nature* 458, 319–321.